J Mater Sci (2012) 47:6151–6165
DOI 10.1007/s10853-012-6535-7

Phase and morphology evolution of calcium carbonate precipitated by carbonation of hydrated lime

Özlem Cizer · Carlos Rodriguez-Navarro · Encarnación Ruiz-Agudo · Jan Elsen · Dionys Van Gemert · Koenraad Van Balen

Received: 21 February 2012 / Accepted: 25 April 2012 / Published online: 11 May 2012

Abstract Phase and morphology evolution of $CaCO_3$ precipitated during carbonation of lime pastes via the reaction $Ca(OH)_2 + CO_2 \rightarrow CaCO_3 + H_2O$ has been investigated under different conditions ($pCO_2 \approx 10^{-3.5}$ atm at 60 % *RH* and 93 % *RH*; $pCO_2 = 1$ atm at 93 % *RH*) using XRD, FTIR, TGA, and SEM. Simulations of the pore solution chemistry for different stages and conditions of carbonation were performed using the PHREEQC code to investigate the evolution of the chemistry of the system. Results indicate initial precipitation of amorphous calcium carbonate (ACC) which in turn transforms into scalenohedral calcite under excess Ca^{2+} ions. Because of their polar character, $\{21\bar{3}4\}$ scalenohedral faces (type S) interact more strongly with excess Ca^{2+} than non-polar $\{10\bar{1}4\}$ rhombohedral faces (type F), an effect that ultimately favors the stabilization of $\{21\bar{3}4\}$ faces. Following the full consumption of Ca^{2+} ions and further dissolution of CO_2 leading to a pH drop of the pore solution, $\{21\bar{3}4\}$ scalenohedra are subjected to dissolution. This eventually results in re-precipitation of $\{10\bar{1}4\}$ rhombohedra at close-to-neutral pH. This crystallization sequence progresses through the carbonated depth with a strong dependence on the degree of exposure to CO_2, which is controlled by the carbonated pore structure governing the diffusion of CO_2. Both the carbonation process and the scalenohedral-to-rhombohedral transformation are kinetically favored under high *RH* and high pCO_2. Supersaturation plays a critical role on the nucleation density and size of $CaCO_3$ crystals. These results have important implications in understanding the behavior of ancient and modern lime mortars for applications in architectural heritage conservation.

Ö. Cizer (✉) · D. Van Gemert · K. Van Balen
Department of Civil Engineering, KU Leuven, Heverlee, Belgium
e-mail: Ozlem.Cizer@bwk.kuleuven.be

C. Rodriguez-Navarro · E. Ruiz-Agudo
Department of Mineralogy and Petrology, University of Granada, Granada, Spain
e-mail: carlosrn@ugr.es

J. Elsen
Department of Earth and Environmental Sciences, KU Leuven, Heverlee, Belgium

Introduction

The reaction between CO_2 and $Ca(OH)_2$ in an aqueous medium, the so-called carbonation, results in the formation of $CaCO_3$ [1, 2]. Carbonation is performed industrially by bubbling CO_2 through a slaked lime slurry (i.e., $Ca(OH)_2$ aqueous suspension) and results in the formation of precipitated calcium carbonate (PCC) which is used as a filler in industrial products [3–9]. Carbonation is also crucial in the setting of traditional lime mortars that have been used as a building material since the advent of pyrotechnology ca. 12000 years ago [10–22]. It is also of importance in the long-term durability of concrete, where $Ca(OH)_2$, i.e., portlandite, is one of the major phases formed during cement hydration [23–26].

Industrial PCC production aims at controlling the phase, morphology, and physical properties (i.e., particle size, aspect ratio, and specific surface area) by adjusting the reactants concentration (i.e., supersaturation) and $[Ca^{2+}]/[CO_3^{2-}]$ ratio, and/or using additives [4–9]. Conversely, carbonation of lime mortars is a natural process that involves the reaction between CO_2 in the atmosphere and $Ca(OH)_2$ (i.e., hydrated and/or slaked lime) in the pore water of the mortar [10, 11]. The setting of traditional lime mortars starts

with an initial step of drying and shrinkage, and is followed by the carbonation reaction which proceeds from the surface into the pore system following several steps: (i) diffusion of gaseous CO_2 through the open pores, (ii) dissolution of $Ca(OH)_2$ in the pore water releasing Ca^{2+} and OH^- ions, (iii) absorption and dissolution of CO_2 in the alkaline pore water forming carbonic acid (H_2CO_3), (iv) its dissociation as bicarbonate (HCO_3^-) and carbonate (CO_3^{2-}) ions, (v) reaction between Ca^{2+} and CO_3^{2-} ions forming $CaCO_3$ through nucleation and subsequent crystal growth [10]. All these processes are interrelated and altering the kinetics of one process influences the others. The overall reaction of lime carbonation can be synthesized as follows [10]:

$$Ca(OH)_2(s) + CO_2(g) \rightarrow CaCO_3(s) + H_2O(aq) + 74\ \text{kJ/mol} \quad (1)$$

The pore structure and the pore water content play an important role in the progress of carbonation in lime mortars by controlling the rate of CO_2 diffusion and the reactants dissolution and concentration, as well as the pore solution supersaturation [11, 17, 26–28]. The supersaturation, in turn, determines the nucleation and growth rates of $CaCO_3$ which acts as a binding agent due to its interconnected microstructure [20].

$CaCO_3$ crystallizes as three polymorphs, calcite, aragonite, and vaterite, depending on the reaction conditions (i.e., pH, *T* and supersaturation), and the presence of impurities or additives [29, 30]. Calcite is the most stable phase at ambient *T* and *P*, and typically displays the $\{10\bar{1}4\}$ rhombohedral habit. However, $\{21\bar{3}4\}$ and $\{21\bar{3}1\}$ scalenohedra, $\{01\bar{1}2\}$ acute rhombohedron, $\{10\bar{1}0\}$ prism, and $\{0001\}$ tabular habits are also observed in nature. In fact, natural calcite is extremely rich in forms and habits, the number of forms exceeding 620 [31]. Aragonite, which typically appears as prisms or needle-like crystals, and vaterite, which tends to form polycrystalline spherulites, are metastable phases and, especially the latter, may play a role as a precursor in calcite formation (Ostwald's rule of stages). Apart from these three polymorphs, metastable amorphous calcium carbonate (ACC) appears as a hydrated transient phase during the initial stages of carbonation at high reactant concentrations [9, 32, 33]. This amorphous phase, which typically appears as small spheres less than 1 μm in diameter, transforms into calcite as the reaction progresses [8, 32]. Some authors suggest that this transformation proceeds via coupled dissolution/precipitation (mass transport) [34, 35], while others have pointed to a solid-state transformation following dehydration at room *T* [36].

$CaCO_3$ precipitation appears to be dependent on the properties of portlandite crystals and on the carbonation conditions (i.e., pore water content, pH and speciation, degree of supersaturation, and ion activity). The role of carbonation conditions on industrially produced PCC have been thoroughly studied with the aim of tailoring PCC yield, particle size and morphology, as well as degree of agglomeration [4–9]. The effects of portlandite crystal size, surface area, and habit on the carbonation of lime mortars have been studied mostly from a kinetic and physical–mechanical point of view [12, 13, 19, 22]. However, little research has focused on the study of the phase, morphology, and microstructure of $CaCO_3$ precipitated during the carbonation of $Ca(OH)_2$ in mortars. Rodriguez-Navarro et al. [22] have shown that ACC is a transient (precursor) phase during lime mortar carbonation. These authors and Cultrone et al. [16] mentioned the precipitation of scalenohedral calcite crystals, i.e., the so-called dogtooth spar [37, 38] during normal (in air) and accelerated (in 100 % CO_2 atmosphere) carbonation of lime mortars, respectively. De Silva et al. [39] reported the precipitation of rhombohedral calcite crystals in compacted lime binders carbonated in CO_2 atmosphere for 6 h. Sanchez-Moral et al. [15] pointed to the influence of *T* on the size of calcite crystals formed in carbonated lime-based mortars. These studies, however, did not offer a complete picture of the evolution of $CaCO_3$ phase and morphology as the carbonation front proceeds from the surface into the mortar. Moreover, they offered no mechanistic interpretation regarding the observed variations in $CaCO_3$ phase and morphology. It should be noted that the physical and mechanical properties of lime mortars largely depend on the phase and textural/microstructural features of the newly formed $CaCO_3$ and its evolution as carbonation progresses [20, 22]. Therefore, the study of the phase and morphology evolution of $CaCO_3$ in lime mortars will be crucial for the evaluation of the behavior of these mortars that are gaining a prominent status as compatible materials in the conservation of the built heritage [12, 19, 21, 22].

The influence of physical properties (particle size and surface area) of portlandite on the phase, size, and morphology evolution of $CaCO_3$ has been discussed in an earlier study in which variations in the phase and morphology $CaCO_3$ along the carbonation depth profile have been established [40]. This article will further focus on the influence of CO_2 concentration and relative humidity (*RH*) which control the pore-water content and evaporation rate, on the formation of $CaCO_3$ on the exposed surface and along the depth profiles of the carbonated lime paste. The aim is to elucidate the mechanism responsible for observed variations in the phase and morphology of $CaCO_3$.

Experimental program

Materials

A commercial lime hydrate, i.e., dry $Ca(OH)_2$ powder, was used. This lime powder is characterized as high-calcium

lime (>90 % $Ca(OH)_2$) with traces of $CaCO_3$ at 5 % by mass. Its particle-size distribution, measured by laser scattering technique with a Malvern Mastersizer using ethanol as a dispersion agent, is in the range of <100 μm with a mean diameter of 6.2 μm. This lime has a high BET-specific surface area ($S_{BET} = 36.2$ m^2/g), determined using Micromeritics Gemini 2360 Surface Area Analyzer, due to the abundance of primary particles with size <100 nm.

Sample preparation

Lime paste was prepared by mixing hydrated lime powder with distilled water to reach 0.37 solid mass ratio. The lime paste was thinly (<1 mm) smeared with a spatula over a sample cup to form a disk of 2 cm in diameter. Such a flat geometry was selected to minimize the diffusion path of CO_2 through the sample thickness, and to insure the 1-D advancement of the carbonation reaction front, i.e., from the exposed upper surface down through the sample depth.

Carbonation

Carbonation in air was carried out under atmospheric conditions (i.e., 20 °C; $pCO_2 \approx 10^{-3.5}$ atm, i.e., the standard concentration of CO_2 in air), and under dry (60 % *RH*) and moist (93 % *RH*) conditions. Accelerated carbonation was carried out using gaseous CO_2 at 100 % volume concentration ($pCO_2 = 1$ atm) under moist conditions (20 °C, 93 % *RH*). No attempt was done to perform accelerated carbonation under dry conditions because the heat evolved during such a fast reaction fully dries the lime paste and hampers its carbonation [10]. Carbonation was carried out in a *RH*-controlled chamber where either air or CO_2 at the desired concentration was introduced. Samples were exposed to carbonation in air for up to 60 days, while the accelerated carbonation in CO_2 atmosphere lasted for 24 h.

Characterization

Precipitated $CaCO_3$ was characterized on a powder X-ray diffractometer (XRD; Philips Analytical) with CuKα radiation generated at 45 kV and 30 mA, 10 and 70° 2θ measuring range, 0.02° 2θ step size and 1.25 s/step counting time. Fourier transform infrared spectroscopy (FTIR) analyses were also performed to identify $CaCO_3$ polymorphs. The analysis was carried out using a Perkin Elmer 1725× spectrometer in the frequency range 400–4000 cm^{-1} with 128 scans/sample and 4.0 cm^{-1} resolution. The degree of carbonation was determined by thermogravimetric analysis (TGA) using a Netzsch STA 409 PC DSC-TGA system in static N_2 atmosphere at a *T* range of 20–1000 °C and at a controlled heating rate of 10 °C/min. The morphology of $CaCO_3$ precipitated on the exposed surfaces and along freshly broken cross-sections (i.e., depth profiles) was investigated using a Philips XL 30S FEG scanning electron microscope (SEM) after coating the samples with gold. To avoid any artifacts resulting from fast diffusion of CO_2 within drying cracks (which were observed in samples carbonated in air at 60 % *RH*), samples were collected from crack-free areas.

Modeling of the pore solution chemistry

Calculation of the lime paste pore solution chemical evolution, speciation, and saturation index SI (SI = log Ω = log (IAP/*Ks*); where Ω is the saturation state of the system, IAP is the ion activity product and K_s is the thermodynamic solubility product of the relevant phase) with respect to the different $CaCO_3$ phases formed during carbonation was performed using the PHREEQC code, which calculates ion activity coefficients using the extended Debye–Hückel equations [41]. In the $CaCO_3$–H_2O–CO_2 system, the PRHEEQC code uses standard equation describing the different equilibria among the components (both ions in solution as well as solid precipitates). Phases considered (and K_s at STP) are portlandite (log $K_s = -5.19$), calcite (log $K_s = -8.48$), and ACC (log $K_s = -6.40$) [42].

Results

Phase analysis

Irrespective of the carbonation conditions, calcite is the only finally formed $CaCO_3$ polymorph identified by XRD (Fig. 1). The presence of uncarbonated portlandite is only

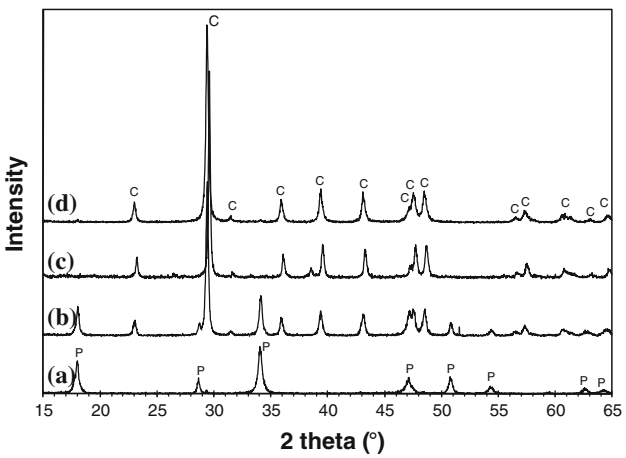

Fig. 1 XRD pattern of the lime hydrate powder (*a*) and the corresponding lime paste carbonated in air ($pCO_2 \approx 10^{-3.5}$ atm) at 60 % *RH* (*b*), in air at 93 % *RH* (*c*), and in a CO_2 atmosphere ($pCO_2 = 1$ atm) at 93 % *RH* (*d*). *P* portlandite, *C* calcite

evident in samples subjected to carbonation in air at 60 % *RH*. These results have been confirmed by FTIR analyses (Fig. 2) showing the characteristic bands of calcite at 711 cm^{-1} (v_4; in-plane bending) and 873 cm^{-1} (v_2: O–C–O out-of-plane bending) [43, 44]. The strong band at ~1423 cm^{-1} ($v3$; asymmetric stretch) and the weak band at ~2508 cm^{-1} ($2v_2 + v_4$) correspond to CO_3^{2-} ions. The strong O–H stretching band at ~3640 cm^{-1} and the H–O–H bending vibration at ~1617 cm^{-1} are due to the presence of $Ca(OH)_2$ which is only present in lime hydrate and lime samples carbonated in air at 60 % *RH* (Fig. 2a–c). In agreement with the XRD analyses, aragonite (~854 and ~1082 cm^{-1}) and vaterite (~745, ~876, ~1085, and ~1600 cm^{-1}) [43, 45] are not observed in the FTIR spectra of the carbonated limes. Interestingly, these spectra show the presence of a broad and/or split band centered at 1423 cm^{-1}, which is particularly broad in the case of the lime paste carbonated in CO_2 atmosphere (Fig. 2e). Such a broad/split

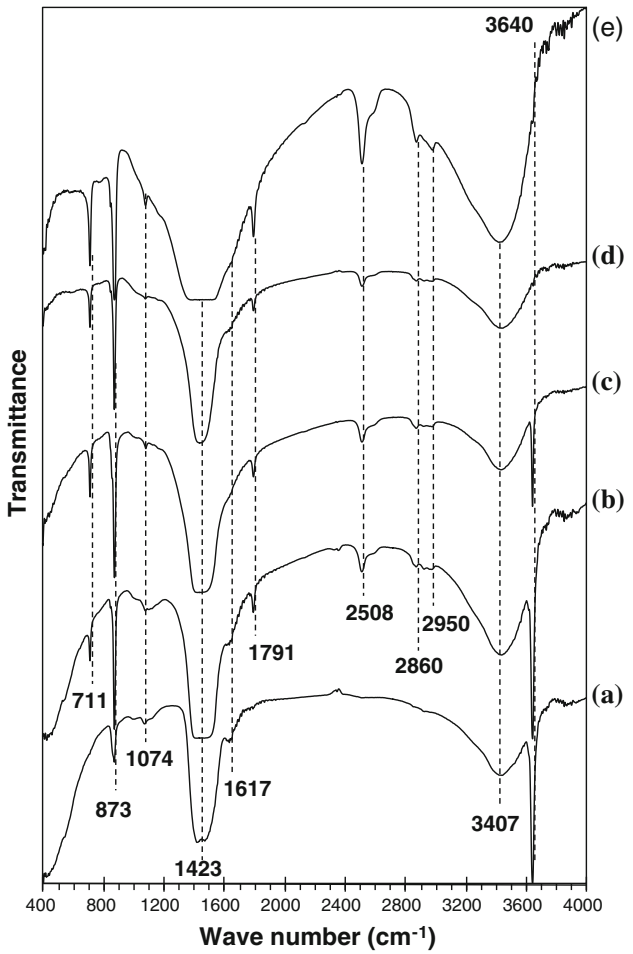

Fig. 2 FTIR spectra of the lime hydrate powder (*a*) and the corresponding lime paste carbonated in air ($pCO_2 \approx 10^{-3.5}$ atm) at 60 % *RH* for 24 h (*b*) and for 60 days (*c*), in air at 93 % *RH* for 60 days (*d*), and in a CO_2 atmosphere ($pCO_2 = 1$ atm) at 93 % *RH* for 24 h (*e*)

v_3 absorption peak is a typical IR feature of ACC [46], and indicates a lack of symmetry in the environment around the CO_3^{2-} ions [47]. The presence of the characteristic ACC absorption band at ~1074 cm^{-1}, which is attributed to the symmetric C–O stretch (v_1) in non-centrosymmetric structures [48], is observed in all carbonated lime pastes. This v_1 band is rather distinctive of ACC [46, 49] and also appears in non-centrosymmetric aragonite and vaterite. Due to its centrosymmetric structure, the band at ~1076 cm^{-1} of calcite is not observed using FTIR; however, such a band can be observed using Raman [47, 50]. FTIR bands corresponding to ACC are stronger in early stages of carbonation (24 h in air at 60 % *RH*) and after carbonation in CO_2 atmosphere (Fig. 2b, e). Note also that the characteristic bands of ACC are already present in the original hydrated lime sample where some $CaCO_3$ is already present due to early carbonation during handling and storage.

TGA plots in Fig. 3 enable the quantification of portlandite (weight loss due to dehydroxylation at 350–450 °C) and $CaCO_3$ (weight loss associated to decarbonation at 650–850 °C) in lime samples carbonated under different conditions. In agreement with the XRD and FTIR results, portlandite is present at 49 wt% in the sample carbonated for 24 h in air at 60 % *RH* (Fig. 3a). With further carbonation up to 60 days under same conditions, the degree of conversion increases with residual portlandite fraction of 15.6 wt% (Fig. 3b). On the other hand, carbonation in air at 93 % *RH* up to 60 days has led to complete conversion of portlandite into $CaCO_3$ (Fig. 3c). This confirms the crucial role of water playing in the carbonation reaction of lime, and is in agreement with macroscale tests [10, 11, 17, 28] as well as nanoscale observations [51, 52]. A nearly complete conversion was achieved after carbonation in CO_2 atmosphere (Fig. 3d). In agreement with FTIR results, TGA plots show weight loss shoulders between ~90 and ~165 °C, which are associated to the release of water present in ACC and a shoulder at ~241 °C corresponding to the transformation of metastable ACC into stable $CaCO_3$ [53, 54]. These particular shoulders are most evident in the lime sample subjected to carbonation in CO_2 atmosphere (Fig. 3d).

Morphology of $CaCO_3$

Carbonation in air at 60 % RH

SEM observations during early stages (24 h) of carbonation show the precipitation of scalenohedral calcite crystals on the exposed surface (Fig. 4a). These crystals typically grow from the {0001} basal surface and, to a limited extent, from $\{10\bar{1}0\}$ and $\{11\bar{2}0\}$ prism faces of portlandite crystals, which display highly porous and

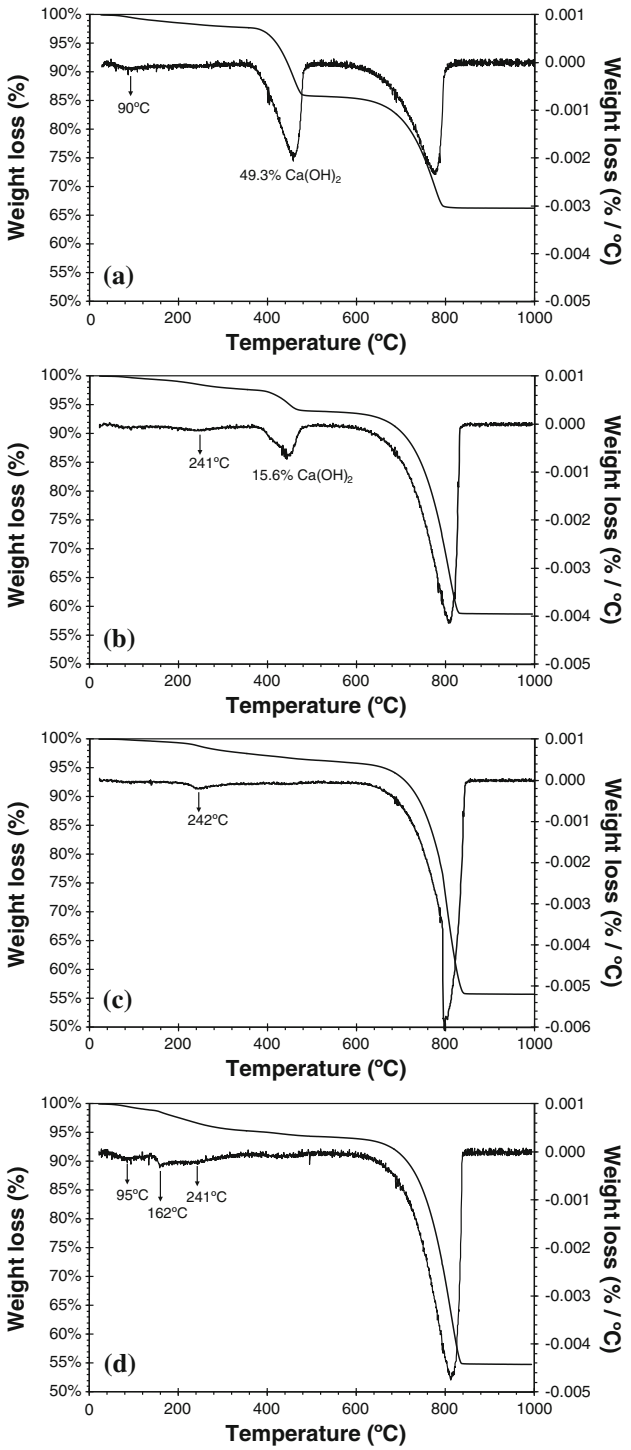

Fig. 3 TGA of lime pastes carbonated under different conditions: **a** $pCO_2 \approx 10^{-3.5}$ atm at 60 % *RH* for 24 h; **b** $pCO_2 \approx 10^{-3.5}$ atm at 60 % *RH* for 60 days; **c** $pCO_2 \approx 10^{-3.5}$ atm at 93 % *RH* for 60 days; **d** $pCO_2 = 1$ atm at 93 % *RH* for 24 h

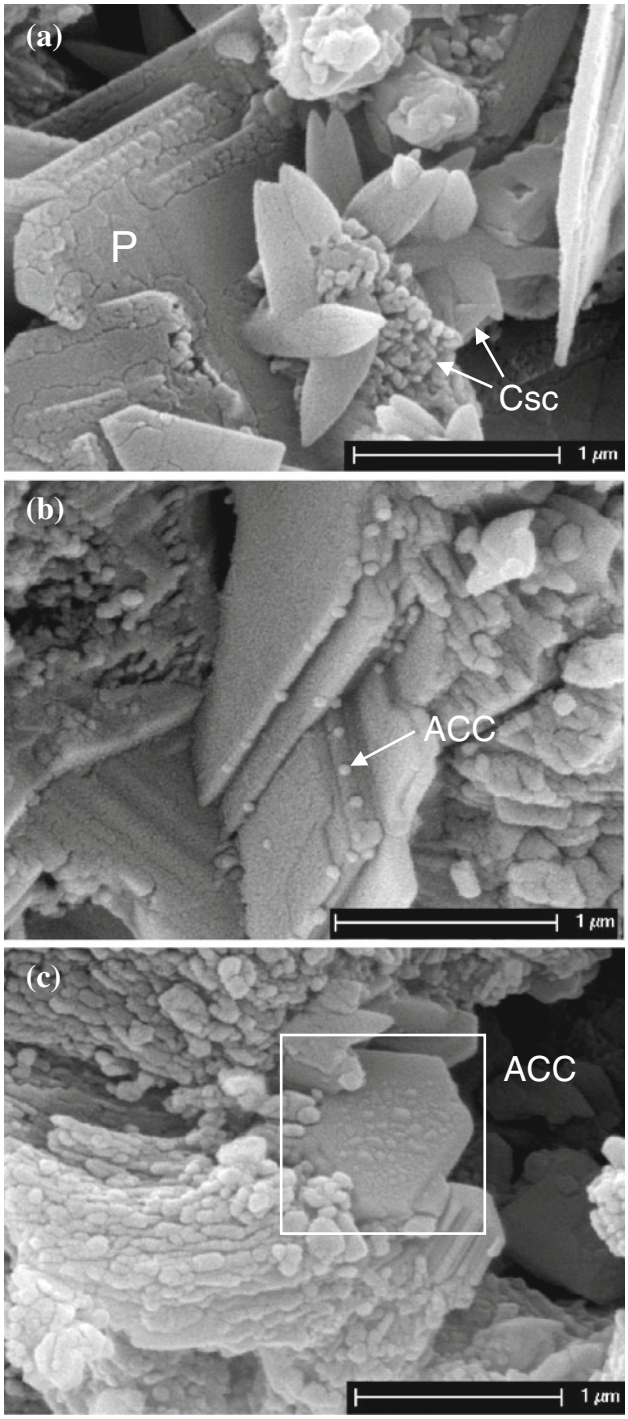

Fig. 4 SEM photomicrographs of lime paste after carbonation in air at 60 % *RH* for 24 h: **a** exposed surface with scalenohedral calcite crystals (Csc) growing from the surface and from the edges of plate-like portlandite crystals (P); **b** ACC on the $\{10\bar{1}0\}$ and $\{11\bar{2}0\}$ prism faces and **c** on the basal {0001} face of portlandite crystals in the depth profile

corroded surfaces indicative of dissolution (Fig. 4a). In the depth profile, abundant portlandite crystals and localized scalenohedral calcite crystals are observed. Interestingly, some plate-like portlandite crystals show nanometer-sized spherules on $\{10\bar{1}0\}$ and $\{11\bar{2}0\}$ prism faces (Fig. 4b) and rough {0001} surfaces (Fig. 4c). Such surface features have been observed at the nanoscale using atomic force

microscope (AFM) and corresponds to the early precipitation of spherulitic $CaCO_3$ [51]. This spherulitic morphology has been associated to the formation of ACC [9, 32, 33].

Further carbonation until 60 days at 60 % *RH* resulted in full precipitation of micrometer-sized scalenohedral calcite crystals on the exposed surface (Fig. 5a). This scalenohedral calcite grows over the portlandite crystals along the depth profile (Fig. 5b, c). As in the case of the lime paste carbonated for 24 h, spherulitic morphologies suggesting the presence of ACC are observed on the portlandite faces in the depth profile (Fig. 5d). These spherulites tend to form chain-like aggregates, similar to the so-called chain-like calcite aggregates observed by Garcia-Carmona et al. [32] in carbonated lime slurries. The authors indicate that such a morphology results from the transformation of ACC nanoparticles, aggregated on the portlandite basal faces, into calcite. Such a transformation is consistent with the FTIR spectra showing a sharpening of the band at 1423 cm^{-1} as carbonation time increased from 24 h to 60 days (Fig. 2b, c).

The basal {0001} faces of the uncarbonated and partially carbonated portlandite crystals in the depth profile display triangular-shaped ridges or pyramids that are typical growth features of portlandite (Fig. 5c) [55]. The surface of both pyramidal/triangular ridges and the basal faces of the portlandite crystals are rough and porous. These observations point toward an initial transformation into $CaCO_3$ via a coupled dissolution/precipitation process, which may eventually lead to a pseudomorphic replacement.

Carbonation in air at 93 % RH

After 60 days of exposure to carbonation in air at 93 % *RH*, calcite crystals formed on the surface are nanometer-sized rhombohedra (Fig. 6a). Such a crystal habit is different from the well-formed scalenohedra precipitated at 60 % *RH* in Fig. 5a. Interestingly, scaleno-rhombohedral crystals at a depth of 20 μm (Fig. 6b) and scalenohedra with corroded/cracked surfaces at the deepest part of ~400 μm are observed along the sample depth profile (Fig. 6c).

Carbonation in CO_2 atmosphere

Micrometer-sized calcite rhombohedra formed on the sample surface directly exposed to the CO_2 atmosphere

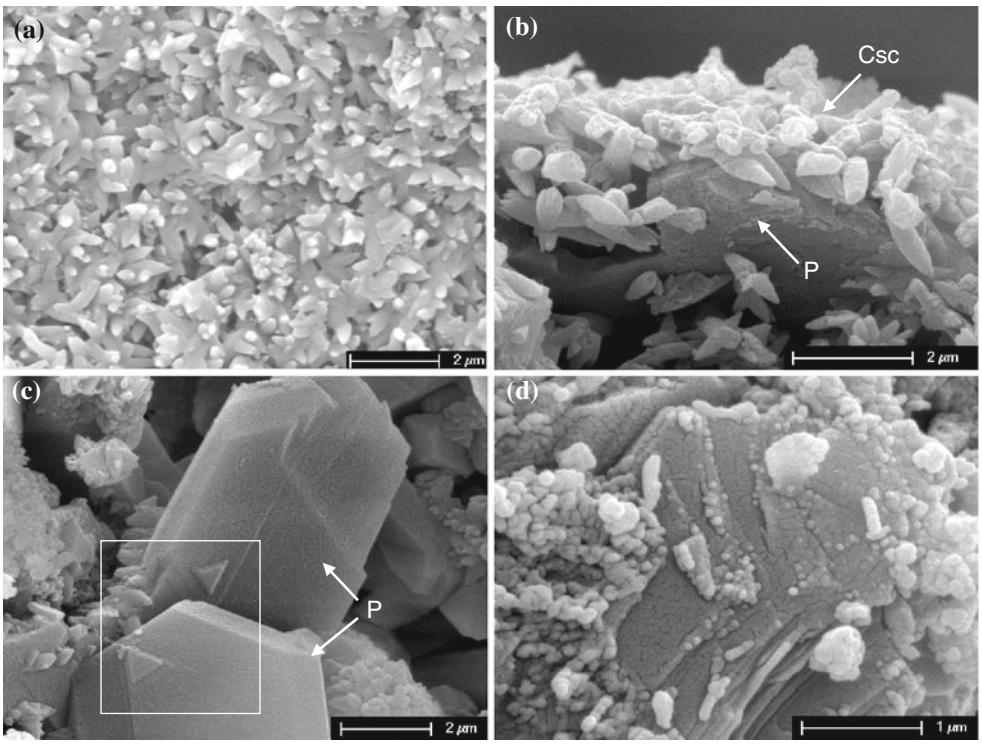

Fig. 5 SEM photomicrographs of the depth profile after carbonation in air at 60 % *RH* for 60 days: **a** scalenohedral calcite crystals on the sample surface; **b** scalenohedral calcite crystals (Csc) growing over a portlandite crystal (P) in a section normal to the surface; **c** scalenohedral calcite crystals growing from the surface and from the edges of plate-like portlandite crystals (P) showing pyramidal/triangular ridges on their basal faces at ~20 μm depth; **d** nanometer-sized calcite spherulites forming chains (chain-like nanocalcite) on the faces of a portlandite crystal (~340 μm depth)

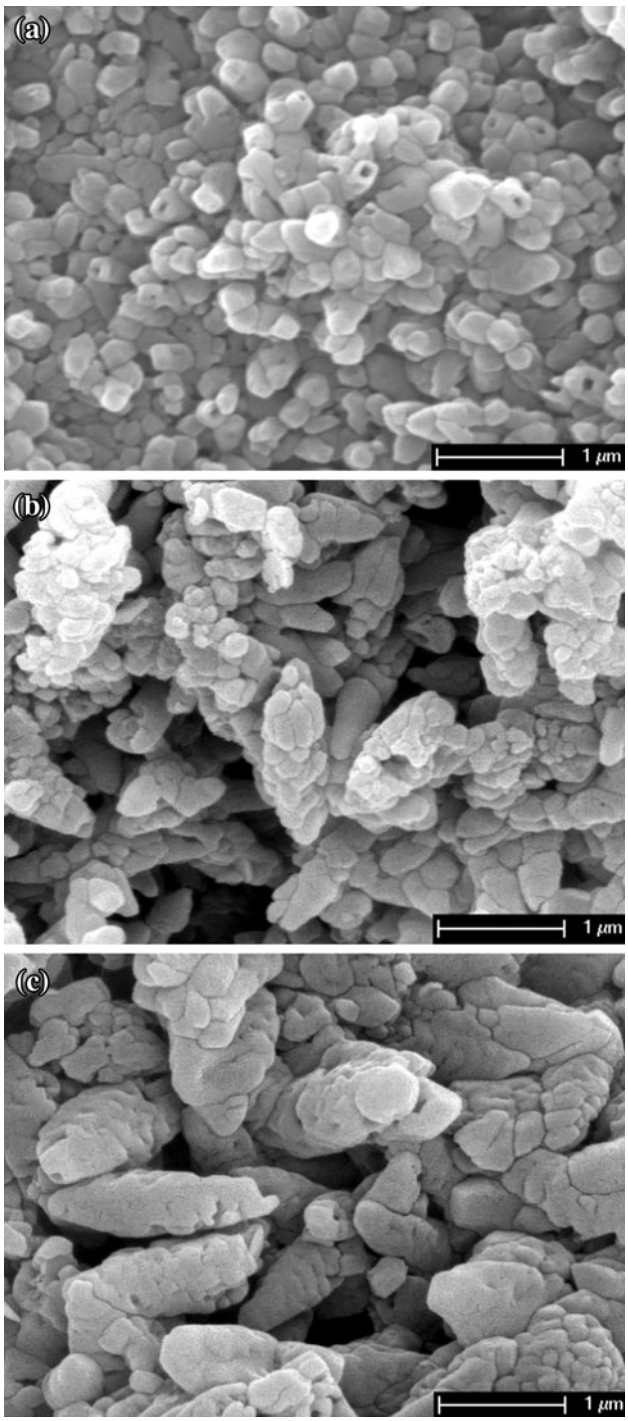

Fig. 6 SEM photomicrograph of **a** nanometer-sized rhombohedra at the exposed surface; **b** scaleno-rhombohedral crystals at a depth of ~20 μm; **c** scalenohedra with corroded/cracked surfaces at the deepest part of ~400 μm after 2-month carbonation in air at 93 % *RH*

(Fig. 7a). Some rhombohedra showed a hopper morphology, similar to that observed by Tai and Chen [56] following calcite crystallization at room *T*, pH 11, and a relatively high supersaturation (SI = 1.9). The high-surface area and reactivity of the lime hydrate seem to favor the formation of calcite at a high supersaturation resulting in hopper crystals [57].

Micrometer-sized rhombohedra formed a 1–2 μm thick surface layer (Fig. 7b). Beneath this surface layer, nanometer-sized rhombohedra forming compact aggregates with stair-case morphology are observed to a depth of ~50 μm (Fig. 7b, c). This second layer is followed by a transition zone from nanometer-sized rhombohedra to nanometer-sized scalenohedra. In the deepest part, only scalenohedral calcite with cracked/corroded surfaces are present (Fig. 7d).

Evolution of the pore solution chemistry

To gain an insight on the evolution of the pore-solution chemistry as carbonation progressed, different simulations were performed using PHREEQC. Simulation 1 considered the case of carbonation in air ($pCO_2 = 10^{-3.5}$ atm) and in a CO_2 atmosphere ($pCO_2 = 1$ atm) under excess $Ca(OH)_2$ maintaining the pH at 12.4 (i.e., the pH of a saturated $Ca(OH)_2$ solution). Simulation 1 thus corresponded to the early stages of the carbonation process. Simulation 2 focused on the analysis of the saturated $Ca(OH)_2$ solution exposed to air and CO_2 atmosphere, once full consumption of solid $Ca(OH)_2$ had occurred. This simulation thus represented the final stage of the carbonation reaction. Simulation 3 evaluated the evolution of the chemistry of the pore water in contact with newly formed calcite crystals and exposed to air and to CO_2 atmosphere. This last simulation strived to show that the chemistry of the system continued to evolve once full carbonation had occurred. In other words, this simulation aimed at explaining why corroded scalenohedral calcite crystals appeared, and why rhombohedral calcite crystals typically appeared at the upper part of the samples.

Table 1 shows the pH, activities of Ca^{2+} and CO_3^{2-}, $[Ca^{2+}]/[CO_3^{2-}]$ activity ratio, and SI with respect to calcite and ACC calculated for each simulation. In simulation 1 the system is supersaturated with respect to the two solid phases. SI values with respect to ACC (SI_{ACC}) and calcite ($SI_{calcite}$) are slightly higher in a CO_2 atmosphere. It has been shown that under similar $SI_{calcite}$ values, growth rates are higher at higher pCO_2 [58]. This is in agreement with the nearly full carbonation reached in our experiments after 24 h exposure to a CO_2 atmosphere. The biggest difference in speciation between the solution equilibrated with $pCO_2 = 10^{-3.5}$ atm and that equilibrated with $pCO_2 = 1$ atm refers to the higher $[Ca^{2+}]/[CO_3^{2-}]$ ratio in the former case. Note that irrespectively of the type of atmosphere, $[Ca^{2+}]/[CO_3^{2-}]$ ratios are always higher than 1 due to the excess Ca^{2+} ions present in the pore solution.

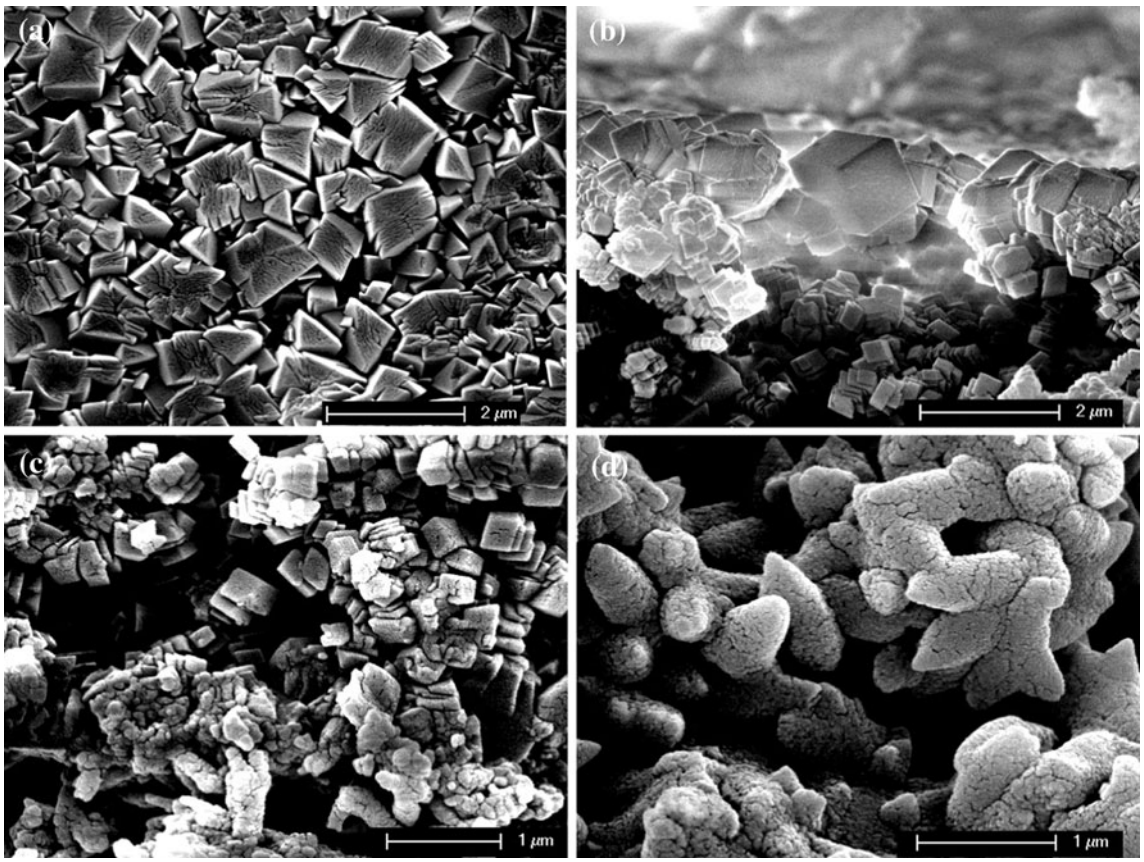

Fig. 7 Variation in calcite crystals morphology along a depth profile after carbonation in CO_2 atmosphere at 93 % *RH*: **a** micrometer-sized rhombohedra at the surface; **b** nanometer-sized rhombohedra (staircase morphology) beneath the surface; **c** transition zone from rhombohedral to scalenohedral morphology (~50 μm depth); **d** scalenohedral calcite crystals with cracked/corroded surface features at the bottom of the sample (~600 μm depth)

Simulation 2 shows that in the case of the solution exposed to air, the pH drops from 12.4 to 9.4, while in the case of a CO_2 atmosphere, the pH drops to 6.3. Such calculated pH drops are consistent with experimental observations during carbonation [59, 60]. These final conditions lead to contrasting SI values. The solution exposed to air shows a $SI > 0$ (i.e., the solution is supersaturated) with respect to all solid phases considered. Conversely, the solution exposed to a CO_2 atmosphere is slightly supersaturated with respect to calcite, but undersaturated with respect to ACC. The latter means that $CaCO_3$ formed as ACC during the initial stages of carbonation should dissolve, and eventually re-precipitate as calcite. This contributes to explaining why little ACC was observed once carbonation was completed upon exposure to a CO_2 atmosphere. Simulation 2 also shows that the $[Ca^{2+}]/[CO_3^{2-}]$ ratio increased by a factor of ca. 750 in the solution equilibrated with a CO_2 atmosphere if compared with the solution equilibrated with air. This is mainly due to a shift in the carbonate/bicarbonate equilibrium as the pH drops.

Simulation 3 shows that exposure of the pore water in contact with calcite to air has resulted in SI values slightly <0 for all phases considered. In this case, the pH has dropped to 7.7. The level of undersaturation is much higher at $pCO_2 = 1$ atm, because the pH has dropped to 4.3. This simulation clearly shows that once carbonation is completed, further exposure to air or CO_2 atmosphere will lead to the dissolution of newly formed $CaCO_3$ in order to neutralize the pore solution. Considering that the kinetics of dissolution of calcite is highly pH-dependent [61] it is expected that a faster and more complete dissolution will take place in a CO_2 atmosphere once carbonation is complete, provided that pore water is still available. Such a dissolution effect will eventually revert to a re-growth process once the pH rises and sufficient Ca^{2+} and CO_3^{2-} ions are present in the solution. New calcite crystals will then precipitate and/or the remaining calcite crystals will re-grow with a morphology in equilibrium with the new pore-solution chemistry (i.e., a pH lower than the original pH 12.4 existing at the initial stages of carbonation). The calculated equilibrium pH values for solutions exposed to air and CO_2 atmosphere, once saturation is reached with respect to calcite ($SI_{calcite} = 0$), are 9.8 and 6.1, respectively.

Table 1 PHREEQC simulations of the evolution of pore solution chemistry under different carbonation conditions

	Simulation 1		Simulation 2		Simulation 3	
pCO_2 (atm)	$10^{-3.5}$	1	$10^{-3.5}$	1	$10^{-3.5}$	1
Final pH	12.4	12.4	9.387	6.306	7.696	4.284
$[Ca^{2+}]$ (mM)	8.37	9.75	4.78	7.75	0.11	0.11
$[CO_3^{2-}]$ (mM)	1.71	4.00	1.34	0.003	5.55×10^{-4}	2.63×10^{-7}
$[Ca^{2+}]/[CO_3^{2-}]$	4.89	2.44	3.58	2.68×10^{3}	2.02×10^{2}	4.24×10^{5}
$SI_{calcite}$	3.64	4.07	3.29	0.83	−1.73	−5.05
SI_{ACC}	1.56	1.99	1.21	−1.26	−3.81	−7.13

An additional experiment was performed to evaluate the validity of the third simulation: calcite scalenohedra was exposed to a 100 % CO_2 atmosphere at 93 % *RH* for 24 h. A drastic morphology change was observed from scalenohedra to scalenohedra showing corroded surface features (Fig. 8a) and their transformation to aggregates of compact nanometer-sized rhomboedral calcite crystals with stair-case habit, similar to that observed in Fig. 7b, c (Fig. 8b).

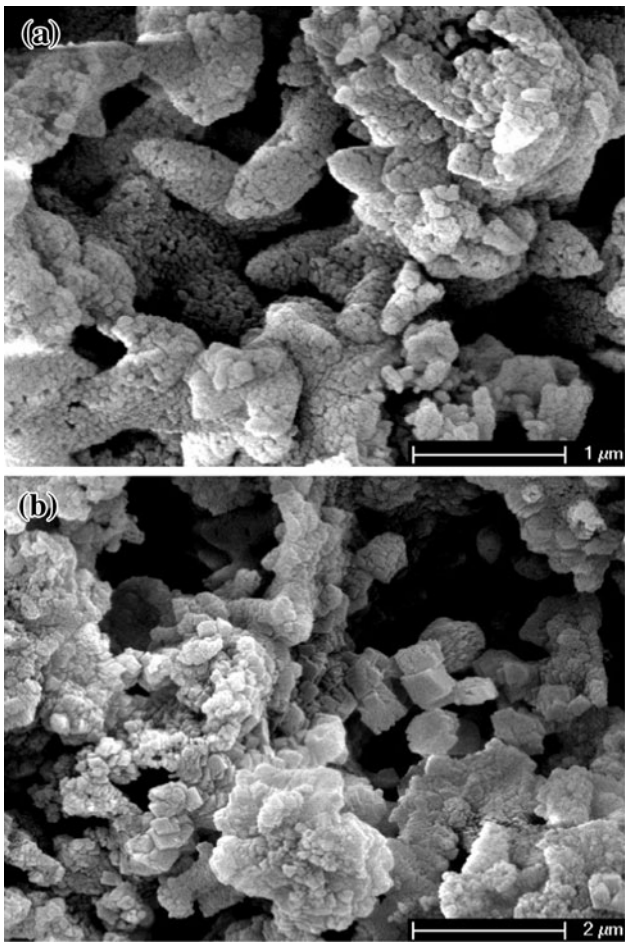

Fig. 8 SEM photomicrographs of scalenohedral calcite crystals after exposure to 100 % CO_2 atmosphere at 93 % *RH*: **a** scalenohedra showing corroded surface features; **b** their transformation (via a dissolution/precipitation process) into nanometer-sized rhombohedra with stair-case morphology

Discussion

Phase evolution

Earlier studies have shown that the crystallization of $CaCO_3$ in solution typically follows the Ostwald's step rule [62]. In the absence of additives and at room *T*, ACC initially precipitates and readily transforms into vaterite and/or calcite [63–67]. The presence of metastable phases preceding the crystallization of calcite is favored by high-supersaturation conditions [65]. High pCO_2 and alkaline pH (8.5–10.5) favor the formation of vaterite, which may eventually transform into stable calcite [56, 68–70]. Conversely, at room *T* and low pCO_2, pH close to neutrality as well as pH > 11 favor the development of calcite crystals [56, 71, 72]. Under the typical high-pH conditions existing during the carbonation of lime pastes, vaterite formation does not seem to be favored. This may be due to the fact that this pH is much higher than 8.5–10.5 which favors the formation of vaterite [56]. It has also been suggested that excess $[Ca^{2+}]$ favors the rapid transformation of vaterite into calcite [59, 73]. Thus, it is plausible that vaterite formed initially and rapidly transformed into calcite in our carbonation experiments due to the high $[Ca^{2+}]/[CO_3^{2-}]$ ratios. However, this is not fully consistent with our FTIR and XRD results showing no vaterite at early and later stages of the carbonation. It is also inconsistent with our observation of spherical nanocrystals and aggregates of ACC formed on the surface of plate-like portlandite crystals. Our results indicate that ACC is the first $CaCO_3$ phase formed in the system as spherical (or hemispherical) nanoparticles which typically precipitate heterogeneously on $Ca(OH)_2$ plates [51]. Following ACC precipitation, the solution supersaturation drops to the solubility of this amorphous phase, and, eventually, this newly formed unstable phase dissolves. Under these conditions the solution will be supersaturated with respect to less soluble

calcite [73]. As a result, calcite will nucleate and grow at the expenses of dissolving ACC. Interestingly, the chain-like aggregates of calcite nanocrystals observed in partially carbonated lime paste in Fig. 5d suggest that in some cases the conversion of ACC to calcite can be a coupled dissolution/precipitation reaction (i.e., pseudomorphic replacement) where morphological aspects of the replaced phase can be preserved in the product phase [74].

Following the formation of calcite after ACC, further dissolution of $Ca(OH)_2$ and CO_2 in the pore water will lead to further calcite growth under high-pH conditions (simulation 1). Once all $Ca(OH)_2$ is consumed (simulation 2), the supply of Ca^{2+} and OH^- will be discontinued. This in turn will result in a pH drop as CO_2 continues to dissolve into the pore water, thus reducing the amount of CO_3^{2-} and increasing the amount of HCO_3^- until a point where growth of calcite should stop. As CO_2 continues to be dissolved in the pore water, the pH will be further reduced and undersaturation with respect to calcite will occur (simulation 3). Dissolution of calcite will thus take place until the pH raises and the concentration of Ca^{2+} and CO_3^{2-} in the pore-water reaches the solubility product of calcite. Eventually, precipitation of newly formed calcite crystals and/or re-growth of the remaining (partially corroded/dissolved) calcite crystals in the pore walls will occur. The dissolution of calcite is strongly dependent on pCO_2 as shown by simulation 3, where final undersaturations of −1.73 (pH 7.69) and -5.05 (pH 4.28) with respect to calcite are reached in air and CO_2 atmosphere, respectively (Table 1). Because the dissolution rate of calcite is proportional to the undersaturation in the system [61], larger quantities of calcite will be dissolved and at a faster rate in the case of the lime paste carbonated in a CO_2 atmosphere if compared with those carbonated in air.

Morphology evolution of calcite crystals

Earlier studies on $CaCO_3$ produced by carbonation routes indicate that supersaturation and $[Ca^{2+}]/[CO_3^{2-}]$ ratio in the solution have a great influence on the habit and polymorph selection [6, 7]. Stoichiometry between Ca^{2+} and CO_3^{2-} ions appears to favor the development of the $\{10\bar{1}4\}$ calcite rhombohedron irrespectively of the supersaturation during calcite crystallization [6, 71]. Conversely, non-stoichiometric conditions with $[Ca^{2+}]/[CO_3^{2-}] \gg 1$ seems to favor the growth of the $\{21\bar{3}4\}$ scalenohedral form under high-pH conditions [6–8]. However, Han et al. [59] report the formation of rhombohedral calcite under excess of Ca^{2+} ions. Note that several researchers [7–9] refer to the $\{21\bar{3}4\}$ scalenohedral form as $\{21\bar{3}1\}$ due to the inconsistent usage of Miller-Bravais indices in terms of the hexagonal structural unit cell ($a = 5$ Å; $c = 17$ Å) and due to the confusion with the hexagonal morphological unit cell ($a = 10$ Å; $c = 8.5$ Å), which was traditionally used to describe calcite twinning, cleavage, and crystal forms [75].

Garcia-Carmona et al. [7, 8] explain the preferential development of scalenohedral calcite crystals during carbonation of lime slurries. On the one hand, the authors state that the rate-limiting step in calcite growth is the dehydration of strongly hydrated Ca^{2+} prior to its incorporation into an active growth site (a kink). Lippman [29] states that a sufficient supply of CO_3^{2-} ions should be the most likely way to overcome this dehydration barrier. In fact, dehydration of metal cations is facilitated by the formation of ion pairs with carbonate groups. Therefore, the formation of $CaCO_3^{\circ}$ neutral ion pairs at the calcite/solution interface is considered as a necessary step in calcite growth. This is in agreement with the recent growth model proposed by Nilsson and Sternbeck [76] indicating that calcite growth rate is controlled by the incorporation of $CaCO_3^{\circ}$ at less abundant $>CaCO_3^{\circ}$ and $>CaHCO_3^+$ surface sites on $\{10\bar{1}4\}$ faces, although the direct incorporation of Ca^{2+} under special conditions is not ruled out. On the other hand, Garcia-Carmona et al. [7, 8] suggest that the smaller Langmurian absorption coefficient of Ca^{2+} ($K_{Ca2+} = 10^6$ cm^3 mol^{-1}) if compared to CO_3^{2-} ($K_{CO_3^{2-}} = 3 \times 10^7$ cm^3 mol^{-1}) does not favor the stoichiometric incorporation of these two ions into the $\{10\bar{1}4\}$ faces of calcite at $[Ca^{2+}]/[CO_3^{2-}]$ ratios equal to unity. Thus, the slow growth normal to these faces contributes to the development of the rhombohedral form. Conversely, at $[Ca^{2+}]/[CO_3^{2-}] \geq 1.2$ equal amounts of Ca^{2+} (as neutral $CaCO_3^{\circ}$ ion pair) and CO_3^{2-} ions could be incorporated into $\{10\bar{1}4\}$ faces, thus favoring their growth and disappearance in the final calcite morphology which is now the scalenohedral form [7, 8]. Although this model provides some insights into the growth of calcite under non-stoichiometric conditions, it shows several shortcomings. For instance, the authors do not explain why of all possible calcite forms, the scalenohedron is the one formed during carbonation of lime slurries by CO_2 bubbling (i.e., conditions where $[Ca^{2+}]/[CO_3^{2-}] > 1$). Note that Nehrke et al. [77] and Tai et al. [78] have shown that the growth rate of calcite is significantly reduced as the growth solution departs from stoichiometry, while in situ AFM observations by Perdikouri et al. [79] show that the rate of step propagation across $\{10\bar{1}4\}$ calcite faces is strongly reduced when $[Ca^{2+}]/[CO_3^{2-}] > 1$. These studies demonstrate that the growth rate of $\{10\bar{1}4\}$ calcite faces is not increased when the $[Ca^{2+}]/[CO_3^{2-}]$ ratio is higher than unity as suggested by Garcia-Carmona et al. [7, 8]; actually, the opposite occurs. Interestingly Perdikouri et al. [79] show that the morphology of growth hillocks formed on the $\{10\bar{1}4\}$

calcite face changes from the typical rhombohedral geometry observed at $[Ca^{2+}]/[CO_3^{2-}]$ ratios close to unity, to a nearly rounded (polygonal) geometry of the obtuse $[\bar{4}41]_+$ and $[48\bar{1}]_+$ steps at $[Ca^{2+}]/[CO_3^{2-}]$ ratios higher (or lower) than one (see Paquette and Reader [80] for a full description of the different growth steps of $\{10\bar{1}4\}$ calcite faces). Note also that these effects are observed at pH $\gg$ 9. These results suggest that the stabilization of faces other than $\{10\bar{1}4\}$, for instance the $\{21\bar{3}4\}$ faces, may occur via interaction of excess (charged) species (here we also include OH^-) with specific growth steps (obtuse steps). In this respect, it has been shown that the alteration in the rate of step propagation along specific directions has a direct impact on the morphology of macroscopic crystals [81]. We suggest that under the typical high-pH conditions existing at the early stages of calcite growth during carbonation of lime pastes, excess Ca^{2+} ions can be adsorbed at the obtuse $[\bar{4}41]_+$ and $[48\bar{1}]_+$ steps of $\{10\bar{1}4\}$ calcite faces. Such an adsorption has been proved by Cicerone et al. [82]. The authors observe that: (i) Ca^{2+} and CO_3^{2-} are the only potential determining ions in the case of calcite; and (ii) under excess Ca^{2+}, the zeta potential is positive at pH > 8.5 (i.e., the isoelectric point of calcite in a saturated solution). This latter result demonstrates that excess Ca^{2+} can in fact be adsorbed on the calcite surface. Such a metal adsorption can be fostered by the presence of abundant OH^- that are strongly hydrated and, hence, can compete for water molecules in the inner sphere hydration shell of Ca^{2+} ions, as it has been described for the case of KCl crystallization at high pH [83]. The presence of abundant OH^- at high pH will favor the dehydration of Ca^{2+} ions and, in turn, their direct adsorption and incorporation at the calcite surface [76].

However, the following question remains unanswered: Why of all possible faces, scalenohedral faces are the ones present in the final growth morphology? There are two plausible, not mutually excluding, explanations. First, one should consider that according to the Hartman and Perdock [84] periodic bond chain (PBC) theory, the faces of a crystal can be classified into three types: (i) F or flat faces, which include at least two PBCs. They grow according to a layer mechanism and growth steps are parallel to PBC directions. F faces are the most stable (less energetic) and typically appear in the growth form of a crystal; (ii) S or stepped faces, which include only one PBC and are less stable than F faces; and (iii) K or kinked faces, which do not contain any PBCs. They grow continuously and do not tend to appear in the growth form of a crystal. The calcite cleavage rhombohedral $\{10\bar{1}4\}$ faces are F faces, while the $\{21\bar{3}4\}$ scalenohedral faces are S faces [72]. The latter faces should not develop as habit-controlling forms [85]. However, if the layer-by-layer growth of $\{10\bar{1}4\}$ faces is hampered by excess Ca^{2+} adsorption at $[\bar{4}41]_+$ and $[48\bar{1}]_+$ obtuse steps, the next most stable faces would be the S faces, that is, the $\{21\bar{3}4\}$ scalenohedral faces. These latter faces can therefore be present in the final calcite growth morphology. On the other hand, to explain the growth of the different calcite forms, one needs to consider the polar or non-polar character of the different calcite faces [86]. The rhombohedral $\{10\bar{1}4\}$ faces are non-polar because they include equal amounts of Ca^{2+} and CO_3^{2-} ions (Fig. 9a, b). Conversely, calcite {0001} faces are polar as they have a dipole moment in the repeating unit perpendicular to the surface (i.e., there is a staking of alternating layers of Ca^{2+} and CO_3^{2-} ions). The scalenohedral $\{21\bar{3}4\}$ faces are also polar, thus having alternating layer with a negative or a positive charge due to the fact that they include non-stoichiometric amounts of Ca^{2+} and CO_3^{2-} ions (Fig. 9c, d). As a consequence, excess counter ions, that is Ca^{2+} (as well as OH^-), will preferentially attach to these charged faces, poisoning their growth, and leading to their development in the final growth form. It could be argued that if an excess ion is present, it should preferentially attach to the highly polar {0001} faces, leading to tabular calcite crystals. However, Lahann [87] suggests

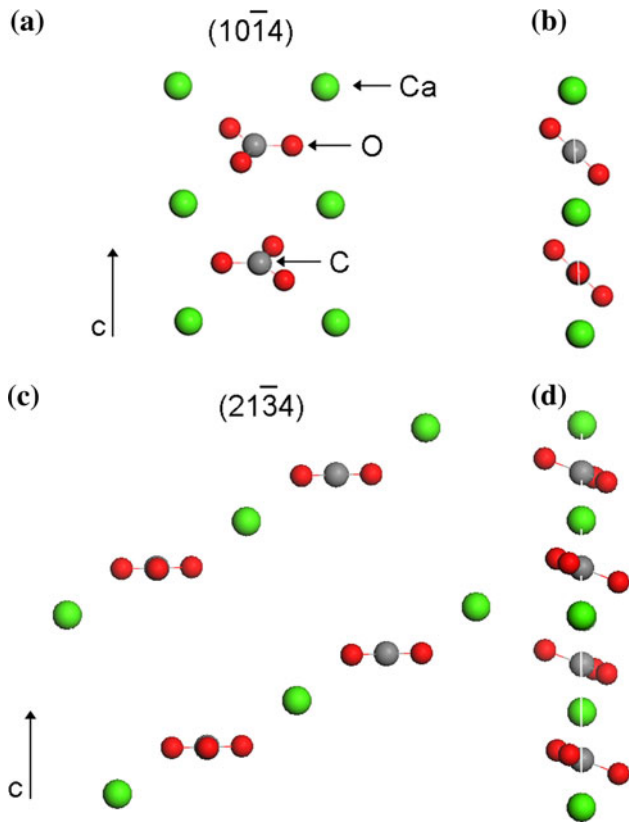

Fig. 9 Structure of calcite $(10\bar{1}4)$ plane (**a**) and its view along the [010] direction (**b**), and the structure of calcite $(21\bar{3}4)$ plane (**c**), and its view along [210] (**d**)

that the development of calcite crystals elongated along the *c* axis is favored under excess Ca^{2+}, because the adsorption of this cation on (0001) planes will render a net positive charging promoting the incorporation of carbonates and resulting in an overdevelopment along the *c* axis. Therefore, a balance is necessary between surface charging and adsorption of excess counter ions, which can only take place in polar faces such as the scalenohedral $\{21\bar{3}4\}$ faces where the dipole moment is not as high as in the {0001} faces. This enables the stabilization of these faces and their overdevelopment in the final calcite growth morphology. Owing to the highly polar character of {0001} calcite faces, their stabilization is only observed following crystallization in the presence of organic molecules with charged headgroups such as sulphonate [60].

A high supersaturation has been claimed as a kinetic factor that may contribute to the stabilization of the scalenohedral form during calcite crystallization [85]. However, while there is a consensus on the fact that rhombohedral morphologies typically develop at a low supersaturation, there are contrasting views as to the role of supersaturation in the development of scalenohedral forms. Jung et al. [6] indicate that the formation of scalenohedral or rhombohedral faces during carbonation of lime is not dependent on the supersaturation. Jung et al. [88] also show that the morphology of calcite crystals is not affected by supersaturation. Conversely, Gonzalez et al. [89] report that rhombohedral calcite crystals develop at a low ($0 < SI < 1$) or high ($1 < SI < 1.3$) supersaturation, while scalenohedral forms develop at a medium/low supersaturation ($SI \sim 1$). Note that, however, these authors report observations in a natural environment (calcite formed in a cave pool) where several effects may affect the morphology of precipitates in an unpredicted way. Interestingly, Tai and Chen [56] show that calcite rhombohedra with hopper faces develop at pH 11 and a SI of 1.9, while at pH 11.5 and a lower SI of 1.6 scalenohedral and rhombo-scalenohedral (football-shaped) calcite crystals form. It follows that supersaturation does not seem to play a critical role in the development of any specific calcite morphology during carbonation of lime pastes. Nevertheless, our results show that the supersaturation plays a critical role on the nucleation density and size of $CaCO_3$ crystals.

For a better understanding of the evolution of phase and morphology of $CaCO_3$ in carbonating lime paste, one should consider the complex nature of this exothermic reaction taking place in a porous system in two main steps: (i) diffusion of the CO_2 gas into the pore structure of the paste and (ii) chemical reaction between the dissolved CO_2 and $Ca(OH)_2$. The presence of water is essential for both reactants dissolution and the progress of the carbonation reaction. However water, which is initially present in the lime paste and is also released during the carbonation reaction (see Eq. (1)), will hamper the CO_2 diffusion within the porous system as the diffusion rate of CO_2 in water is a few orders of magnitude lower than in air. Van Balen [17] has reported that the CO_2 diffusion coefficient increases almost linearly from capillary water content at fresh state, where the water system is continuous enough to hinder the diffusion of CO_2, toward dry mortar state depending on the nature of the pore system and *RH* conditions. Therefore, the carbonation rate will depend on the drying (evaporation) rate, capillary transport regime and capillary condensation [11, 17, 90]. During the early stages the carbonation reaction only takes place on the surface of the fresh lime paste due to the strong resistance against CO_2 diffusion by the capillary water. This is consistent with observations of scalenohedral calcite crystals appearing only at the exposed surface but not in the sample depth after 24 h of carbonation in air at 60 % *RH* (Fig. 4). The chemical reaction will advance from the surface inside the paste as water evaporates due to drying, which is fostered by the exothermic nature of the carbonation reaction, leaving a network of unsaturated pores behind for CO_2 to diffuse. Note that evaporation of water is also facilitated by the hydrophobic character of $CaCO_3$ crystals, implying that water will tend to leave the reaction site once $CaCO_3$ precipitates even at high-*RH* conditions [20, 52]. Therefore, evaporation of the pore water takes place during the carbonation of the lime paste, the rate of which depends on *RH* and *T* conditions and on the characteristics of the pore network. Evaporation occurs much faster at 60 than at 93 % *RH*; thus, a faster evaporation rate in the former conditions has led to the observed incomplete conversion of portlandite (Figs. 1b, 2c, and 3b). This evaporation behavior will induce two phenomena that might play a role in the phase and morphology evolution of $CaCO_3$. The first one is the development of shrinkage microcracks due to the fast evaporation during carbonation of the lime paste at 60 % *RH*. This implies that CO_2 can diffuse into the structure through these microcracks without following the 1-D advancing reaction front. This probably influenced the overall carbonation reaction kinetics which is not the scope of this study. Conversely, crack formation has a negligible effect on the phase and morphology of $CaCO_3$. Calcite crystals precipitating both at the surface and in the sample depth profile at 60 % *RH* (carbonation in air) show the same scalenohedral morphology (Fig. 5). Since shrinkage microcracks were not observed in the lime pastes carbonated at 93 % *RH* in air and in CO_2 atmosphere, we can rely on the 1-D diffusion path of CO_2 from the surface into the structure in these two cases.

The second phenomenon induced by the evaporation is the flux of the water vapor from the bottom toward the

surface of the lime paste. This will influence the amount of liquid water phase remaining in the depth profile and, therefore, the amount of dissolved CO_2 which can reduce the pH of the pore water once the carbonation reaction is completed. This last effect is at the core of the observed phase and morphology variation of calcite. Taking this into account we can deduce that following the early precipitation of ACC, scalenohedral calcite precipitates at high pH as the reaction front penetrates within the lime paste. As CO_2 continues to diffuse into the structure from the surface at 93 % *RH*, which assures the presence of liquid water phase, less stable and more soluble scalenohedral calcite will be subjected to dissolution due to the reduced pH. This will favor the transition from scalenohedral-to-rhombohedral calcite via a dissolution/precipitation process at the surface and near-to-surface areas which are exposed completely and for longer periods of time to CO_2 (Figs. 6a, 7a–c). As a consequence, the less exposed deeper parts only show scalenohedral calcite with cracked/corroded surface features due to the CO_2 diffusion/dissolution controlled mechanism (Fig. 6b, c, 7d). For the same reason, rhombohedral calcite predominates in samples carbonated in a CO_2 atmosphere than in those carbonated in air. These results clearly suggest that the scalenohedral-to-rhombohedral transformation is kinetically favored under high *RH* and high pCO_2.

It is well established that lime mortars prepared using lime with a high surface area develops Liesegang patterns as periodic layers of precipitated $CaCO_3$ with the initial precipitation of ACC followed by its transformation into calcite [3, 22]. The phase, morphological, and textural evolution of $CaCO_3$ observed here may have strong implications on the Liesegang pattern development in carbonating lime mortars as compatible materials for the repair and conservation of historic masonry. In addition, the fact that forced carbonation, artificially intensified carbonation process at high pCO_2, has significant impacts on the phase and morphological features of $CaCO_3$ should be taken into account when mechanical properties, pore structure and microstructure of lime mortars and calcium-silicate systems (such as cement mortar and concrete) cured under such conditions are investigated. This is particularly relevant in the case of carbonation of cement wells during underground CO_2 injection and sequestration [91].

Conclusions

RH conditions and pCO_2 have a significant effect on the phase, morphology, habit, and size of $CaCO_3$ formed during carbonation of lime paste, as well as in their phase evolution. Formation of ACC on $Ca(OH)_2$ crystals occurs at the initial phase of carbonation, followed by its dissolution and re-precipitation as $\{21\bar{3}4\}$ scalenohedra under excess Ca^{2+} ions and at high pH. The formation of the non-equilibrium scalenohedral morphology is explained considering the role of (excess) Ca^{2+} and OH^- ions present in the pore solution in contact with solid $Ca(OH)_2$ (pH 12.4). OH^- ions contribute to the dehydration of Ca^{2+} ions thus favoring their adsorption at the calcite/solution interface. Owing to their polar character, $\{21\bar{3}4\}$ faces (type S) interact more strongly with excess Ca^{2+} than (lowest energy) non-polar $\{10\bar{1}4\}$ faces (type F), an effect that ultimately favors the stabilization of $\{21\bar{3}4\}$ faces in the growth morphology of calcite crystals first formed.

Calcite morphology has been found to vary with the carbonation depth and, therefore, with the exposure time to CO_2, from rhombohedra at the exposed surface (longer CO_2 exposure time), scalenohedra with cracked/corroded surface features along the carbonated depth profile, and scalenohedra with smooth faces in the deepest part (shorter CO_2 exposure time). $\{21\bar{3}4\}$ scalenohedra transforms into $\{10\bar{1}4\}$ rhombohedra via a dissolution/precipitation process associated with the pH drop taking place upon $Ca(OH)_2$ consumption and further CO_2 dissolution into the pore water. Both the carbonation process and the scalenohedral-to-rhombohedral transformation are kinetically favored under high *RH* and pCO_2. Carbonation can also take place via coupled dissolution/precipitation replacement of $Ca(OH)_2$ crystals by calcite pseudomorphs. These results indicate that phase and morphological evolution of $CaCO_3$ may have strong implications in the ultimate performance of lime mortars and other technological processes such as CO_2 sequestration.

Acknowledgements KU Leuven and Research Foundation - Flanders (FWO) are gratefully acknowledged for funding the research. CRN and ERA acknowledge funding provided by the Spanish Government under grant MAT2006-00578 and by EU Initial Training Network Delta-Min (Mechanisms of Mineral Replacement Reactions) grant PITN-GA-2008-215360. The Getty Conservation Institute (GCI), Los Angeles, USA is gratefully acknowledged for the BET analysis. This study was a part of the Lime Mortars and Plasters project, a collaborative research effort among the GCI, University of Granada and KU Leuven.

References

1. Gillott JE (1967) J Appl Chem 17:185
2. Boynton RS (1981) Chemistry and technology of lime and limestone. Wiley, New York
3. Yagi H, Iwazawa A, Sonobe R, Matsubara T, Hikita H (1984) Ind Eng Chem Fundam 23:153
4. Uebo K, Yamazaki R, Yoshida K (1992) Adv Powder Technol 3:71
5. Chen PC, Tai CY, Lee KC (1997) Chem Eng Sci 52:4171

6. Jung WM, Kang SH, Kim WS, Choi CK (2000) Chem Eng Sci 55:733
7. Garcia-Carmona J, Gomez Morales J, Rodriguez Clemente R (2003) J Coll Interface Sci 261:434
8. Garcia-Carmona J, Gomez Morales J, Rodriguez Clemente R (2003) J Crystl Growth 249:561
9. Domingo C, Loste E, Gómez-Morales J, García-Carmona J, Fraile J (2006) J Supercritical Fluids 36:202
10. Moorehead DR (1986) Cem Concr Res 16:700
11. Van Balen K, Van Gemert D (1994) Mater Struct 27:393
12. Rodriguez-Navarro C, Hansen EF, Ginell WS (1998) J Am Ceram Soc 81:3032
13. Cazalla O, Rodriguez-Navarro C, Sebastián E, Cultrone G (2000) J Am Ceram Soc 83:1070
14. Elert K, Rodriguez-Navarro C, Pardo ES, Hansen E, Cazalla O (2002) Stud Conserv 47:62
15. Sanchez-Moral S, Garcia-Guinea J, Luque L, Gonzalez-Martin R, Lopez-Arce P (2004) Mater Constr 54:23
16. Cultrone G, Sebastian E, Ortega Huertas M (2005) Cem Concr Res 35:2278
17. Van Balen K (2005) Cem Concr Res 35:647
18. Hansen EF, Van Balen K, Rodriguez-Navarro C (2005) In: International building lime symposium. National Lime Association, Orlando
19. Hansen EF, Rodriguez-Navarro C, Van Balen K (2008) Stud Conserv 53:9
20. Beruto DT, Barberis F, Botter R (2005) J Cult Herit 6:253
21. Van Balen K, Papayianni I, Van Hees R, Binda L, Waldum A (2005) Mater Struct 38:781
22. Rodriguez-Navarro C, Cazalla O, Elert K, Sebastián E (2002) Proc Royal Soc Lond A 458:2261
23. Verbeck GJ (1958) In: Cement and concrete. ASTM special technical publications no. 205. ASTM, Baltimore
24. Richardson MG (1988) Carbonation of reinforced concrete: its causes and management. Citis Ltd, Dublin
25. Taylor HFW (1997) In: Cement chemistry. Thomas Telford Publishing, London
26. Papadakis VG, Vayenas CG, Fardis MN (1991) ACI Mater J 88:363
27. Saetta AV, Schrefler BA, Vitaliani RV (1995) Cem Concr Res 25:1703
28. Van Balen K, Van den Brande C, Toumbakari EE, Van Gemert D (1997) In: 10th International congress on the chemistry of cement, Amarkai AB and Congrex Goteborg AB, Gothenburg, 4IV010
29. Lippman F (1973) In: Sedimentary carbonate minerals. Springer-Verlag, New York
30. Rodriguez-Navarro C, Jimenez-Lopez C, Rodriguez-Navarro A, Gonzalez-Muñoz MT, Rodríguez-Gallego M (2007) Geochim Cosmochim Acta 71:1197
31. Kostov I, Kostov RI (1997) In: The habit of minerals. MIR Publications, Moscow
32. Garcia-Carmona J, Morales JG, Sáinz JF, Loste E, Clemente RR (2004) J Cryst Growth 262:479
33. Elfil H, Roques H (2001) Desalination 137:177
34. Aizenberg J, Muller DA, Grazul JL, Hamann DR (2003) Science 299:1205
35. Pontoni D, Bolze J, Dingenouts N, Narayanan T, Balleuff M (2003) J Phys Chem B 107:5123
36. Ajikumar PK, Wong LG, Subramanyam G, Lakshminarayanan R, Valiyaveettil S (2005) Cryst Growth Des 5:1129
37. Haüy RJ (1784) In: Essai d′une theorie sur le structure des crystaux appliquée à plusieurs genre de substances crystallisées, VIII 236. Gogué et Née de la Rochelle Libraires, Paris
38. Kashkai MA, Aliev RM (1970) Miner Mag 37:929
39. De Silva P, Bucea L, Moorehead DR, Sirivivtananon V (2006) Cem Conc Comp 28:613
40. Cizer Ö, Van Balen K, Elsen J, Van Gemert D (2008) In: Baciocchi R, Costa G, Polettini A, Pomi R (eds) 2nd International conference on accelerated carbonation for environmental and materials engineering, Rome
41. Parkhurst DL, Appelo CAJ (2000) In: U.S. Geological Survey Water-Resources Investigation Report 99-4259
42. Brečević L, Nielsen AE (1989) J Cryst Growth 98:504
43. Gadsden JA (1975) In: Infrared spectra of minerals and related inorganic compounds. Butterworths, New York
44. Taylor DR, Crowther RS, Cozart JC, Sharrock P, Wu J, Soloway RD (1995) Hepathology 22:488
45. Wang C, Zhao J, Zhao X, Bala H, Wang Z (2006) Powder Technol 163:134
46. Aizenberg J, Lambert G, Weiner S, Addadi L (2002) J Am Chem Soc 124:32
47. Addadi L, Raz S, Weiner S (2003) Adv Mater 15:959
48. Farmer VC (1974) In: The infrared spectra of minerals. Mineralogical Society, London
49. Koga N, Yamame Y (2008) J Therm Anal Calorim 94:379
50. Gunasekaran S, Anbalangan G, Pandi S (2006) J Raman Spectrosc 37:892
51. Yang T, Keller B, Magyari E, Hatmetner K, Günther D (2003) J Mater Sci 38:1909. doi:10.1023/A:1023544228319
52. Beruto DT, Botter R (2000) J Eur Ceram Soc 20:497
53. Koga N, Nakagoe Y, Tanaka H (1998) Thermochim Acta 318:239
54. Xu X, Tark Han J, Kim DH, Cho K (2006) J Phys Chem B 110:2764
55. Tadros ME, Skalny J, Kalyoncu RS (1976) J Coll Interface Sci 55:20
56. Tai C, Chen FB (1998) AIChE J 44:1790
57. Sunagawa I (1981) Bull Mineral 104:81
58. Reddy M, Plummer LN, Busenberg E (1981) Geochim Cosmochim Acta 45:1281
59. Han YS, Hadiko G, Fuji M, Takahashi M (2006) J Mater Sci 41:4663. doi:10.1007/s10853-006-0037-4
60. Page MG, Cölfen H (2006) Cryst Growth Des 6:1915
61. Morse JW, Arvidson RS (2002) Earth Sci Rev 58:51
62. Ogino T, Suzuki T, Kawada K (1987) Geochim Cosmochim Acta 51:2757
63. Clarkson JR, Price TJ, Adams CJ (1992) J Chem Soc, Faraday Trans 88:243
64. Kawano J, Shimobayashi N, Kitamura M, Shinoda K, Aikawa N (2002) J Cryst Growth 237–239:419
65. Kitamura M (2002) J Cryst Growth 237–239:2205
66. Kim WS, Hirasawa I, Kim WS (2004) Ind Eng Chem Res 43:2650
67. Andreassen JP (2005) J Cryst Growth 274:256
68. Spanos N, Koutsoukos PG (1998) J Phys Chem B 102:6679
69. Dickinson SR, Henderson GE, McGrath KM (2002) J Cryst Growth 244:369
70. Hadiko G, Han YS, Fuji M, Takahashi M (2005) Mater Lett 59:2519
71. McKauley JW, Roy R (1974) Am Miner 59:947
72. Heijnen WMM (1985) N Jb Miner Mh 8:357
73. Sawada K (1997) Pure Appl Chem 69:921
74. Putnis A (2002) Miner Mag 66:689
75. Hazen RM (2006) Am Miner 91:1715
76. Nilsson Ö, Sternbeck J (1999) Geochim Cosmochim Acta 63:217
77. Nehrke G, Reichart GJ, Van Cappellen P, Meile C, Bijma J (2007) Geochim Cosmochim Acta 71:2240
78. Tai CY, Chang MC, Wu CK, Lin YC (2006) Chem Eng Sci 61:5346

79. Perdikouri C, Putnis CV, Kasioptas A, Putnis A (2009) Cryst Growth Des 9:4344
80. Paquette J, Reeder RJ (1995) Geochim Cosmochim Acta 59:735
81. Kowacz M, Putnis A (2008) Geochim Cosmochim Acta 72:4476
82. Cicerone DS, Regazzoni AE, Blesa MA (1992) J Coll Interface Sci 154:423
83. Mohameed HA, Ulrich J (1996) Cryst Res Technol 31:27
84. Hartman P, Perdock WG (1955) Acta Cryst 8:49
85. Searl A (1991) J Sediment Petrol 61:195
86. Duffy DM, Harding JH (2004) Langmuir 20:7637
87. Lahann RW (1978) J Sediment Petrol 48:337
88. Jung T, Kim WS, Choi CK (2004) Cryst Growth Des 4:491
89. Gonzalez LA, Carpenter SJ, Lohmann KC (1992) J Sediment Petrol 62:382
90. Houst YF, Wittmann FH (1994) Cem Concr Res 24:1165
91. Regnault O, Lagneau V, Schneider H (2009) Chem Geol 265:113